The Upper-Ocean Response to Surface Heating

CRAIG M. LEE*

School of Oceanography, University of Washington, Seattle, Washington

DANIEL L. RUDNICK

Scripps Institution of Oceanography, La Jolla, California

(Manuscript received 8 June 1994, in final form 30 May 1995)

ABSTRACT

Moored observations of atmospheric variables and upper-ocean temperatures from the Long-Term Upper-Ocean Study (LOTUS) and the Frontal Air–Sea Interaction Experiment (FASINEX) are used to examine the upper-ocean response to surface heating. FASINEX took place between January and June 1986 at 27°N, 70°W while LOTUS took place between May and October 1982 at 34°N, 70°W. The frequency-domain transfer function between rate of change of heat and the net surface heat flux is consistent with a one-dimensional heat balance between heating and convergence of vertical turbulent heat flux at timescales longer than the inertial. The observations satisfy the vertically integrated one-dimensional heat equation and indicate that the response to surface heating has been successfully isolated. Within the internal waveband, upward phase propagation in the response is inconsistent with a one-dimensional balance and the vertically integrated heat balance fails. The internal waveband response is explained as a balance between rate of change of heat, mixing, and vertical advection. A simple model, which admits internal waves forced by an oscillatory surface buoyancy flux, illustrates the competition between these three terms. Stratification modulates the depth to which surface heating is mixed. The estimated eddy diffusivity may be considered a linear function of frequency where the scaling constant reflects the mixed layer depth.

1. Introduction

Vertical mixing and advection transfer momentum, heat, and other oceanic properties into the mixed layer and below. Moored observations of wind velocities and upper-ocean currents have produced a sequence of descriptions of wind-driven momentum transfer into the upper ocean. Observations during the Mixed Layer Experiment (MILE) (Davis et al. 1981b), the Long-Term Upper-Ocean Study (LOTUS) (Price et al. 1987; Schudlich and Price 1995), and the Frontal Air–Sea Interaction Experiment (FASINEX) (Rudnick and Weller 1993b; Weller et al. 1991) have verified the Ekman transport relationship and characterized the vertical momentum flux as a wind-driven current spiral. An examination of how heat penetrates into the upper ocean provides a complementary view of mixing. The goal of this analysis is to isolate the upper-ocean response to forcing by surface heat flux using moored observations of atmospheric variables and upper-ocean temperatures from LOTUS and FASINEX. We understand the observations using the one-dimensional model described below and a simple model we introduce in section 4, where upper-ocean temperature is driven by turbulent heat flux and vertical advection of the background stratification.

In one-dimensional mixed layer models, radiation and wind-driven mixing transfer heat into the upper ocean (Price et al. 1986). Early observations of upper-ocean temperature and surface heating (Bowden et al. 1970; Davis et al. 1981a; Halpern and Reed 1976; Shonting 1964) show that under all but calm wind conditions the vertical heat flux profile is determined more by mixing than radiation absorption and penetrates well below the $O(1\ \text{m})$ predicted by irradiance models (Paulson and Simpson 1977). The competing effects of wind mixing and stratification govern the vertical penetration of solar heating. Even in the presence of strong horizontal variability, Rudnick and Weller (1993a) suggest the applicability of a one-dimensional model by showing that surface heat flux dominates the volume-integrated heat budget of the upper 40 m at diurnal and semidiurnal frequencies.

Consider a one-dimensional heat balance (Sverdrup et al. 1942), in which the turbulent heat flux is parameterized using a constant eddy diffusivity

* Current affiliation: Department of Physical Oceanography, Woods Hole Oceanographic Institution, Woods Hole, Massachusetts.

Corresponding author address: Dr. Craig M. Lee, Department of Physical Oceanography, Woods Hole Oceanographic Institution, Woods Hole, MA 02543.

$$\frac{\partial T}{\partial t} = K\frac{\partial^2 T}{\partial z^2}. \tag{1.1}$$

Here temperature $T(z, t)$ is a function of depth and time, z is positive upward, K is a constant eddy diffusivity, and advective effects and horizontal mixing are neglected. This is analogous to the classic Ekman equation for wind-driven flow in the upper ocean. Assuming a solution $T(z, t) = \tilde{T}(z, \omega)e^{i\omega t}$ to (1.1) forced by an oscillatory surface heat flux, $Q_0(t) = \tilde{Q}_0(\omega)e^{i\omega t}$ yields a result identical to that for the time-dependent Ekman spiral (Faller and Kaylor 1969) with ω replacing $f + \omega$:

$$\tilde{T}(z, \omega) = T_0 \exp\left[(1 + i)\sqrt{\frac{\omega}{2K}}z\right] \tag{1.2}$$

$$T_0 = \frac{(1 - i)\tilde{Q}_0}{\rho_0 c_p\sqrt{2K\omega}}. \tag{1.3}$$

Here $\rho_0 c_p$ is the specific heat capacity of seawater, and we define heat flux as positive downward to maintain the analogy with Ekman dynamics. This produces a heating spiral in the complex plane identical in shape to the Ekman spiral where turning with depth represents changes in phase. A hodograph of $\partial T/\partial t = i\omega\tilde{T}$ (Fig. 1) illustrates the solution where positive (negative) phase means the heating leads (lags) the surface heat flux. Clockwise (anticlockwise) turning of the phase vector with depth indicates downward (upward) phase propagation. At the surface, rate of change of temperature leads surface heat flux by $\pi/4$, and the phase spiral turns clockwise and decays smoothly with depth. Vertically integrating (1.1) from below the influence of surface heating to the surface and applying the flux condition $K\partial T/\partial z = Q_0/\rho_0 c_p$ at $z = 0$ results in

$$\rho_0 c_p \int_{-\infty}^{0} \frac{\partial T}{\partial t}\,\partial z = Q_0. \tag{1.4}$$

This is an analog of the Ekman transport relation and states that all of the surface heating appears as a change in heat content within the water column. As (1.4) requires only that the heat balance be one-dimensional, it is a robust result, independent of the parameterization of the turbulent flux.

Previous investigations (Bowden et al. 1970; Halpern and Reed 1976; Shonting 1964; Sverdrup et al. 1942) focused on estimating eddy diffusivities from upper-ocean temperature data and (1.1)–(1.3) without isolating the response to surface heating from variability in upper-ocean temperature due to other sources. Identification of temperature fluctuations forced by surface heating requires dependable estimates of surface heat flux and sufficient degrees of freedom to reliably extract the desired signal from noise due to sources such as internal waves. Long, moored time series of atmospheric variables and upper-ocean temperatures provide an ideal dataset with which to approach this problem. The challenge here is similar to that faced by Chereskin and Roemmich (1991), Davis et al. (1981b), Price et al. (1987), Rudnick and Weller (1993b), Schudlich and Price (1995), and Weller et al. (1991) in identifying directly wind-driven flow and verifying the Ekman transport relationship. Isolating the response to surface heating has several advantages. The largest source of noise in the analysis of directly wind-driven flow is geostrophic shear, with advection playing a smaller role. In contrast, only the advective terms of the heat equation contribute noise to a similar analysis for surface heating, and the signal to noise ratio should be higher. Additionally, the daily cycle of heating and cooling provides an energetic, distinct forcing signal. The analysis is also insensitive to wind-driven mooring motion, which complicates the identification of high-frequency wind-driven flow (Rudnick and Weller 1993b).

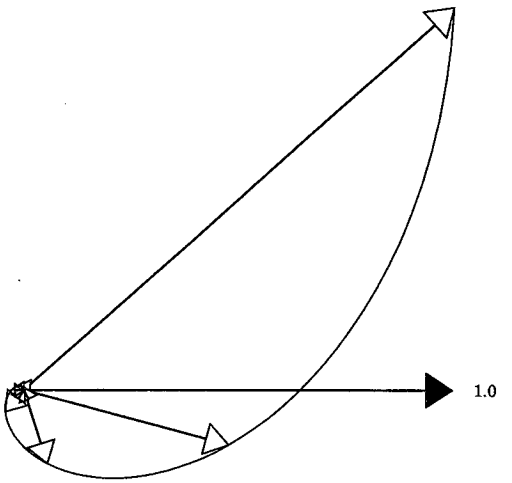

FIG. 1. Hodograph of $\partial T/\partial t$ scaled by $D/Q_0 = (2K/\omega)^{1/2}/Q_0$ from the analytical model (1.1)–(1.3) forced by surface heat flux. The horizontal arrow with the solid tip is a unit vector in the direction of the real axis. Hollow-tipped vectors mark the solution at integral nondimensional depths $z' = z(\omega/2K)^{1/2}$ between 0 and 20, and the curve connecting the tips traces $\partial T/\partial t$ as a function of depth. Anticlockwise (clockwise) displacement relative to the solid-tipped scale vector indicates $\partial T/\partial t$ leads (lags) Q_0. The size of the arrow heads decreases with depth. The response is a phase spiral in the complex plane with downward phase propagation and amplitude decaying with depth.

We address the problem of identifying upper-ocean response to surface heating using data from LOTUS and FASINEX described in section 2. The response is isolated and found to be inconsistent with a simple balance between rate of change of heat and mixing in section 3. In section 4, we explain this result using a simple, analytic model where mixing and vertical advection balance rate of change of heat. We examine the diffusivities and length scales implied by the observa-

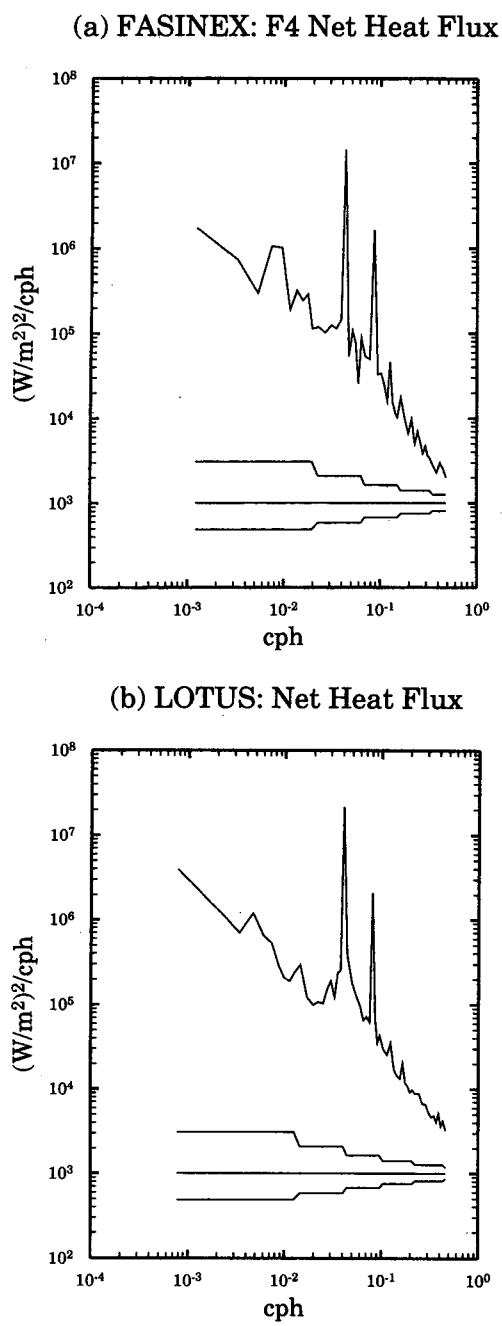

FIG. 2. Power spectra of net surface heat flux for (a) FASINEX mooring F4 and (b) LOTUS. The 95% confidence intervals are calculated following Bendat and Piersol (1986) and plotted below the spectra.

tions and models in section 5 and present conclusions in section 6.

2. Data

This study uses moored observations from the western North Atlantic taken during LOTUS and FASINEX. Both experiments provide time series of upper-ocean temperature accompanied by meteorological observations from which heat fluxes may be estimated.

FASINEX took place from January to June 1986, near 27°N, 70°W in the North Atlantic Subtropical Convergence Zone. We use data from five surface moorings [F2, F4, F6, F8, and F10, see Weller et al. (1991) for a schematic] with typical horizontal separations of 20 km. Each mooring carried a meteorological recorder and a vector averaging wind recorder (VAWR) on a surface buoy and a combination of vector measuring (VMCM) and vector averaging (VACM) current meters at depths of 10, 20, 30, 40, 80, 120, and 160 m (Weller et al. 1990a,b). Temperature sensors at 40 m (F6) and 80 m (F10) failed to return usable records. The hourly average data span 102 days, the longest common interval for which observations are available at all moorings, and terminate just before a significant change in upper-ocean stratification around mid-May.

Data from LOTUS consists of records from a single mooring deployed at 34°N, 70°W between May and October of 1982 (Briscoe and Weller 1984; Deser et al. 1983). Atmospheric data were collected by a VAWR mounted on the surface buoy, and upper-ocean temperature measurements were obtained from VMCMs at depths of 5, 10, 15, 20, 25, 35, 65, 75, and 100 m. We use 160 days of hourly average data spanning the entire LOTUS-3 deployment.

3. Observations

The goal of this analysis is to isolate changes in upper-ocean temperature forced by surface heating. We pose a one-dimensional balance between rate of change of heat and convergence of turbulent heat flux and use a statistical model to identify the upper-ocean response to surface heating during FASINEX and LOTUS.

a. Heat flux and upper-ocean temperature

We calculate FASINEX net surface heat flux for each mooring from records of wind velocity, insolation, relative humidity, barometric pressure, and air and sea surface temperature (Weller et al. 1991). Temperatures at 10, 20, 30, 40, 80, 120, and 160 m are taken from current meter records, with additional measurements at 1 m from thermistors mounted on the surface buoys. Errors in the net heat flux are of $O(50\ \mathrm{W\ m^{-2}})$ and upper-ocean temperature errors are 0.1°, 0.01°, and 0.2°C for the 1-m, near-surface, and thermocline measurements, respectively (Weller et al. 1990a; Weller et al. 1990b). Surface heat flux at mooring F4, near the center of the array, is representative of conditions during FASINEX. The daily cycle of heating and cooling, modulated by the passage of weather systems on timescales of a few days, drives heat flux variability. Power spectra of the F4 net heat flux (Fig. 2a) reveal promi-

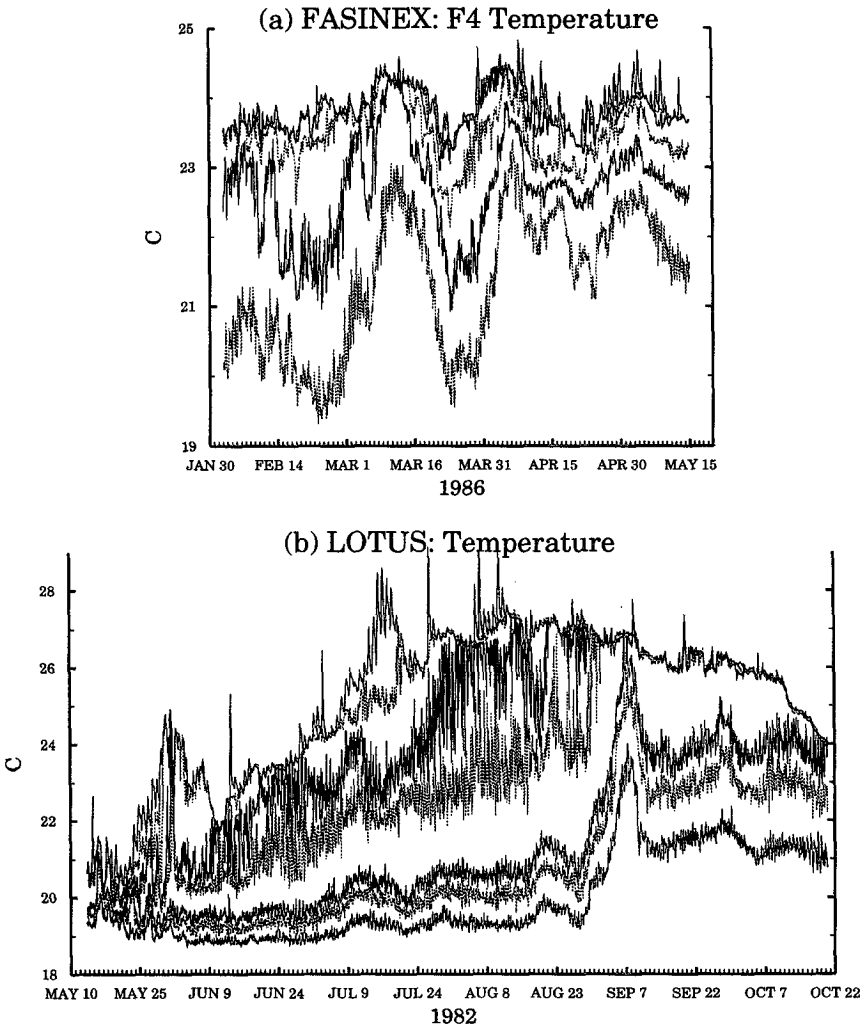

FIG. 3. Temperatures for (a) FASINEX mooring F4 and (b) LOTUS. Traces represent temperatures at 1, 20, 40, 80, 120, and 160 m for FASINEX and 1, 10, 25, 35, 65, 75, and 100 m for LOTUS.

nent peaks at the diurnal and semidiurnal frequencies as well as a smaller peak centered around 4 days.

Frontal passages dominate the FASINEX temperature record (Fig. 3a) on timescales longer than 10 days, with stratification in the seasonal thermocline weakening over the course of the experiment. A comparison of power spectra of net heat flux (Fig. 2a) with spectra of rate of change of heat, $\rho_0 c_p \partial T/\partial t$ (Fig. 4a) suggests a response to diurnal heating, where $\rho_0 c_p = 4.1 \times 10^6$ J m^{-3} °C^{-1} and the time derivative is calculated using centered first differences. At 1 m, $\rho_0 c_p \partial T/\partial t$ has prominent peaks at the diurnal and semidiurnal frequencies, corresponding to the strong diurnal cycle of surface heat flux. By 40 m, these peaks have disappeared. In their investigation of the FASINEX heat budget, Rudnick and Weller (1993a) find that surface heating plays a prominent role in the volume-integrated budget of the upper 40 m and suggest that a one-dimensional model is appropriate. In contrast, horizontal advection dominates both deeper in the water column and at frontal timescales.

Following Deser et al. (1983), we calculate net heat flux for LOTUS from VAWR winds, insolation, barometric pressure, air, and sea surface temperature. Relative humidity (RH) was not measured during LOTUS-3 and is instead estimated using the climatological mean of RH = 75% from Isemer and Hasse (1985). An error of ΔRH = 5% results in an error in the latent heat flux of ΔQ_E = 19 W m^{-2} (Weller et al. 1990a), and estimation of the latent heat flux contributes the largest source of error to the net heat flux. A downward bias of 60 W m^{-2} in the LOTUS-3 insolation measurements (Deser et al. 1983) has not been corrected as it has only a minor effect primarily on the mean response.

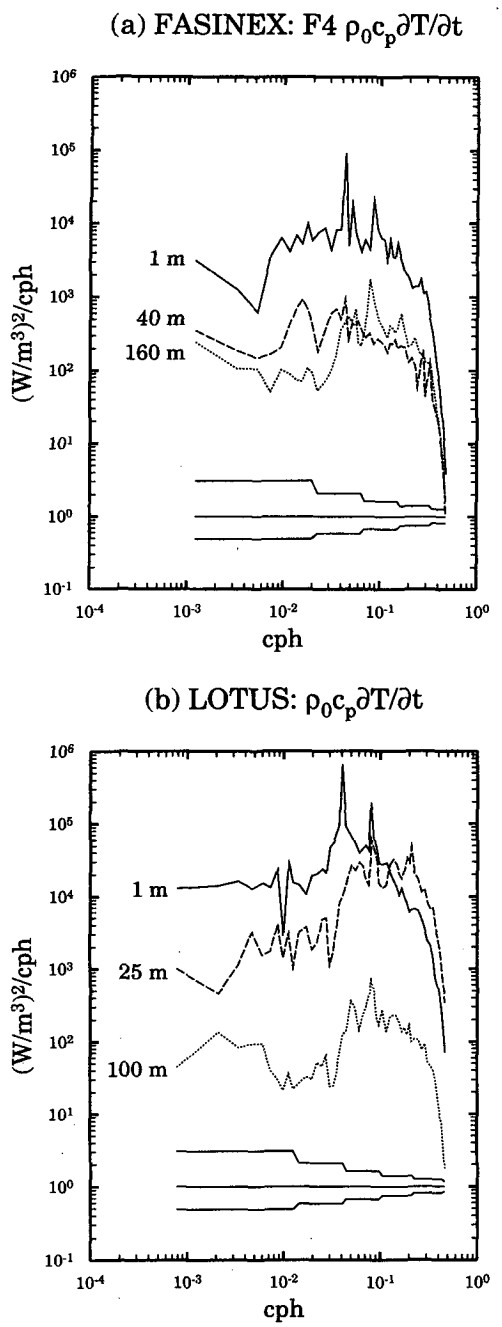

FIG. 4. Power spectra of heat rate of change for (a) FASINEX mooring F4 at 1 (solid), 40 (dashed), and 160 (dotted) m and (b) LOTUS at 1 (solid), 25 (dashed), and 100 (dotted) m. Spectra for the two deepest records in each diagram are offset down one and two decades, respectively. The 95% confidence intervals are plotted beneath the spectra.

Total net heat flux random error is approximately 113 W m^{-2}, and temperature errors are similar to those in FASINEX. Net heat flux decreases as the year progresses but is otherwise dominated by the diurnal cycle. For example, power spectra (Fig. 2b) display peaks at the diurnal and semidiurnal frequencies.

During LOTUS, the upper 35 m of the water column warms steadily through mid-August, and the mixed layer deepens over the course of the experiment (Fig. 3b). Temperatures in the seasonal thermocline increase only slightly during the first two-thirds of the record, with an abrupt warming accompanied by a strengthening of the stratification in early September. Power spectra of $\rho_0 c_p \partial T/\partial t$ (Fig. 4b) show peaks corresponding to surface heating at 1 m, but by 20 m these are no longer apparent.

We calculate buoyancy frequencies for FASINEX and LOTUS from temperature records using a linear equation of state and an expansion coefficient of $\alpha = 2.7 \times 10^{-4}$ K^{-1} (P = 1 atm, S = 35 psu, and T = 22°C). Depth-averaged buoyancy frequency is 5.5 $\times 10^{-3}$ s^{-1} for FASINEX and 1.1 $\times 10^{-2}$ s^{-1} for LOTUS.

b. Observed response to surface heating

Neglecting advection and horizontal mixing, the linear heat equation is a balance between the rate of change of heat and vertical convergence of turbulent heat flux. Based on this one-dimensional heat equation, we choose a model to isolate the response to surface heating

$$\rho_0 c_p \frac{\partial T}{\partial t}(z, \omega) = H_Q(z, \omega) Q_0(\omega) + n(z, \omega), \quad (3.1)$$

where $\partial T/\partial t(z, \omega)$ is calculated from centered first differences of observed temperatures, $Q_0(\omega)$ is the observed surface heat flux, and $n(z, \omega)$ is noise assumed to be incoherent with $Q_0(\omega)$. The complex transfer function $H_Q(z, \omega)$ has units of per meter and is

$$H_Q(z, \omega) = \rho_0 c_p \frac{\left\langle Q_0^*(\omega) \frac{\partial T}{\partial t}(z, \omega) \right\rangle}{\langle Q_0^*(\omega) Q_0(\omega) \rangle}, \quad (3.2)$$

where angle brackets indicate averaging over frequency bands and asterisks denote complex conjugation. We define the rate of change of heat coherent with the observed surface heat flux as $\rho_0 c_p \partial \hat{T}/\partial t = H_Q Q_0$.

Consider the complex transfer function $H_Q(z, \omega)$ as a hodograph in the complex plane, where the magnitude indicates the size of surface-forced changes in heat content. If the heat balance were exactly (1.1), the transfer function would be equal to $i\omega\rho_0 c_p \tilde{T}(z, \omega)/\tilde{Q}_0$ (Fig. 1). Temperature response, rather than its time derivative, may be considered by rotating $H_Q(z, \omega)$ 90° clockwise in the complex plane and dividing by frequency.

We derive a test of the vertically integrated, one-dimensional heat balance by substituting the modeled rate of change of heat (3.1) into (1.4),

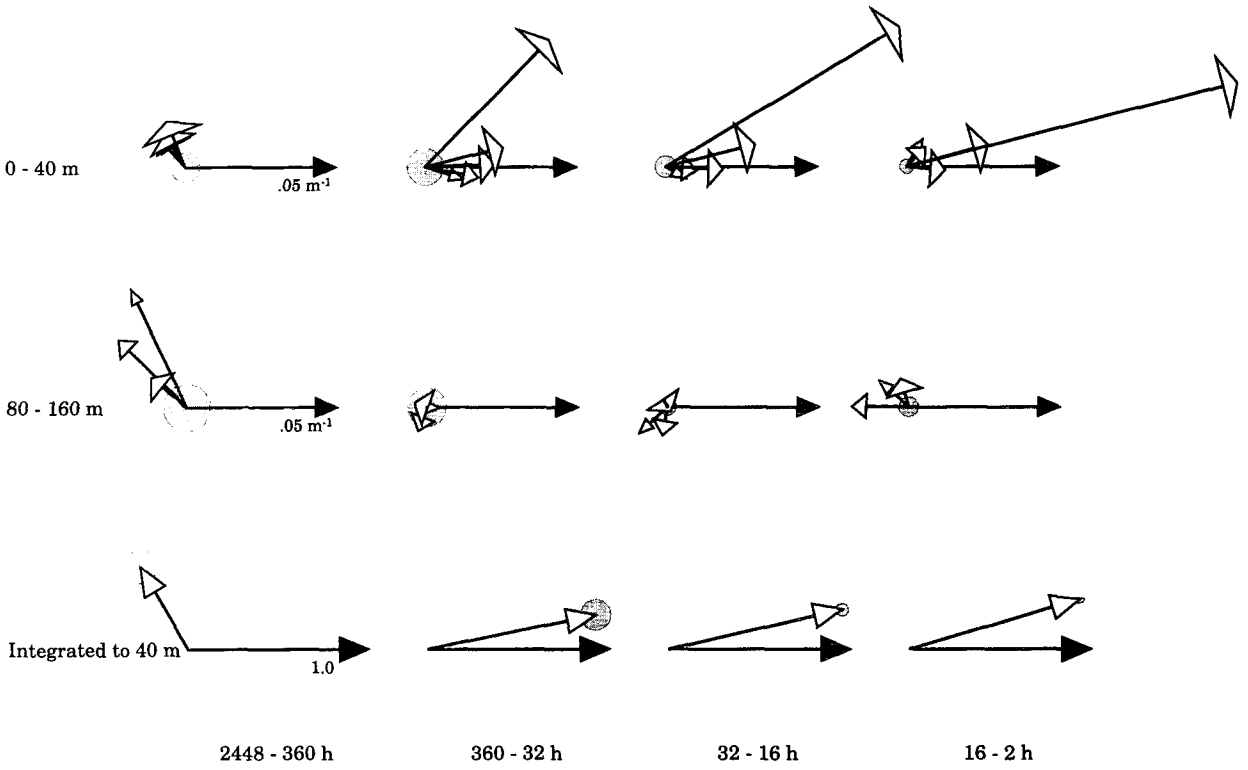

FIG. 5. Hodographs of the FASINEX transfer function between $\rho_0 c_p \partial T/\partial t$ and Q_0. The four columns correspond to the response for timescales between 2448 and 360, 360 and 32, 32 and 16, and 16 and 2 h. In the top two rows, solid-tipped horizontal-scale arrows indicate 0.05 m^{-1} in the direction of the real axis. The transfer function is plotted in two depth groupings as hollow-tipped arrows, where the top row includes depths of 1, 10, 20, 30, and 40 m and the middle row shows depths of 80, 120, and 160 m. Within each grouping, arrowhead size decreases with depth. Transfer function integrated from 40 m to the surface is displayed in the bottom row. Here, the solid-tipped scale arrow is a unit vector in the direction of the real axis, and the hollow-tipped vector is the vertically integrated response. Standard random errors are plotted as gray circles for the shallowest estimate in each grouping in the top two rows and for the vertically integrated response in the bottom row.

$$\int_{-h}^{0} H_Q(z, \omega)\partial z = 1. \qquad (3.3)$$

If the heat balance is strictly between the rate of change of heat and vertical convergence of turbulent heat flux and all the heating has been isolated, we expect the transfer function to integrate to unity when $z = -h$ is beneath the depth to which turbulent heat flux extends. If the dynamics are truly one-dimensional, (3.3) must be satisfied. Failure of the vertically integrated heat balance suggests that a one-dimensional model cannot fully describe the response.

Averaging over frequency bands and, for FASINEX, over the five moorings yields transfer function estimates for periods between 2448 and 360, 360 and 32, 32 and 16, and 16 and 2 h for FASINEX and 3840 and 360, 360 and 32, 32 and 16, and 16 and 2 h for LOTUS. Frontal variability dominates the low-frequency band in FASINEX, where the heat balance is primarily between the rate of change of heat and horizontal advection. The next lowest frequency band encompasses variability due to weather systems, while diurnal and semidiurnal variability dominate the highest frequency bands. Hodographs compactly represent the transfer function and its vertical integral (Figs. 5 and 6). Each column corresponds to a frequency band and the top two rows represent shallow (top row) and deep (middle row) depth groupings. The left margin displays depth ranges for each group while the arrowhead size indicates depth within a group, with the largest head being the shallowest depth and the smallest the deepest. The solid-tipped, horizontal-scale arrow indicates 0.05 m^{-1} (FASINEX) or 0.1 m^{-1} (LOTUS) in the direction of the real axis. Phase differences between the hodographs (rate of change of heat) and the scale vectors (surface heat flux) illustrate the phase structure of

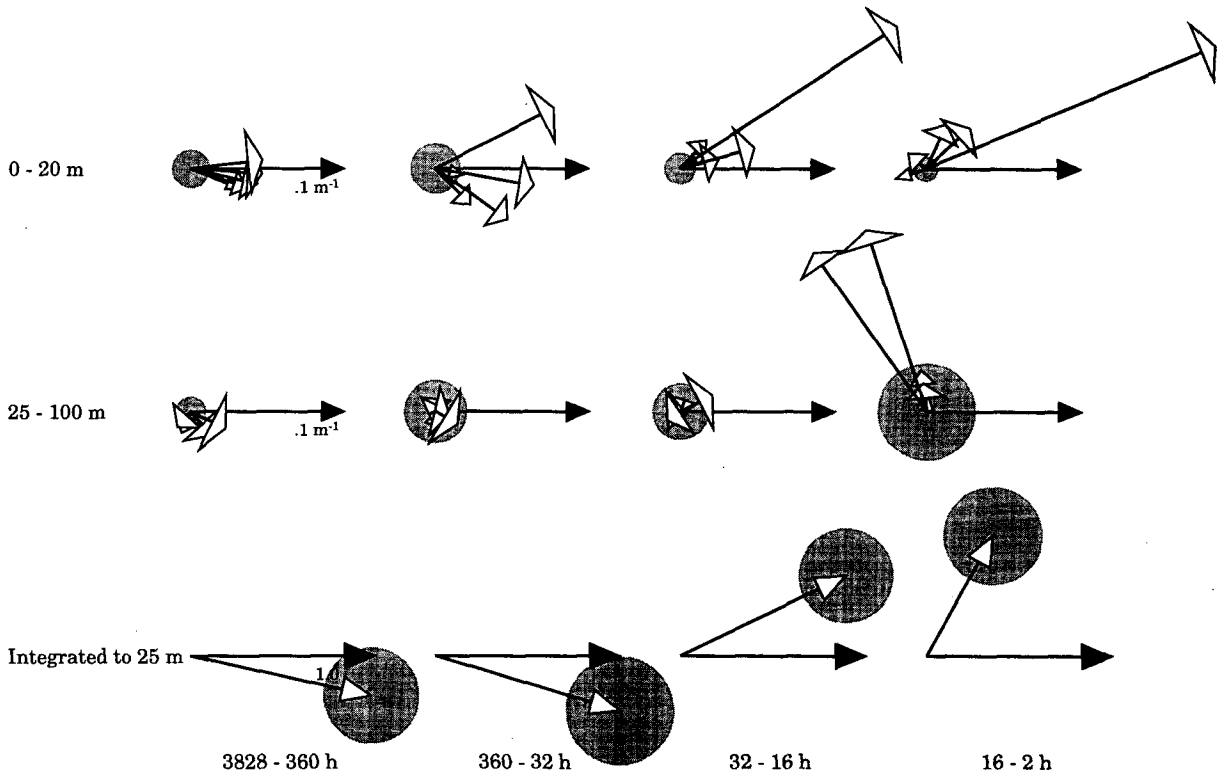

FIG. 6. Hodographs of the LOTUS transfer function between $\rho_0 c_p \partial T/\partial t$ and Q_0. Except as noted, the description of Fig. 5 applies. The four columns correspond to the response for timescales between 3828 and 360, 360 and 32, 32 and 16, and 16 and 2 h. Note the change in scale arrows from 0.05 m^{-1} in Fig. 5 to 0.1 m^{-1} here. The two depth groupings are now 1, 5, 10, 15, and 20 m and 25, 35, 65, 75, and 100 m. Transfer function integrated from 25 m to the surface is displayed in the bottom row.

the observed response. The bottom row contains vertically integrated transfer functions, where the depth of integration is indicated and the scale vector has a real value of 1.0 (unitless). Gray circles mark the size of the standard random error (Bendat and Piersol 1986) for the shallowest estimate in each grouping and for the integrated response. The increased degrees of freedom provided by multiple moorings in FASINEX result in smaller random errors.

At all timescales the observed response is surface intensified, with differences in penetration depths between the two experiments reflecting differences in stratification. FASINEX response is essentially limited to the upper 40 m while that in LOTUS is trapped above 25 m.

At periods longer than 360 h, the model succeeds in isolating the response to surface heating for LOTUS, although it fails to do so for FASINEX. During LOTUS, a smooth clockwise spiral is present and the depth-integrated response is, within a standard error, 1.0. Satisfaction of the integrated heat balance suggests that response to surface heating is fully described by (3.1). In contrast, the FASINEX transfer function maintains a near-constant phase of approximately $2\pi/3$, decays little with depth, and results in depth-integrated heating that is smaller than the surface flux and has a phase of $2\pi/3$. The response is not consistent with a one-dimensional heat balance. Frontal and eddy variability dominates the low-frequency band where the balance is primarily between the rate of change of heat and horizontal advection (Rudnick and Weller 1993a). Wind stress and heat flux are coherent at these frequencies, and the response seen here may be due to wind-driven horizontal advection coherent with the surface heat flux.

Transfer functions for periods between 360 and 32 h for both experiments display smooth, clockwise turning phase spirals that decay rapidly with depth. Vertically integrated heating is within one and two standard errors of unity for LOTUS and FASINEX respectively. Both depth-integrated heating and vertical structure of the response are consistent with a one-dimensional balance between the rate of change of heat and vertical convergence of turbulent heat flux.

Response in the diurnal band is surface intensified but, particularly in LOTUS, fails to exhibit a smooth phase lag with depth. Integrated heating leads the surface heat flux by a margin larger than two standard errors in FASINEX and is barely within two standard errors of unity for LOTUS. Energetic forcing by the daily cycle of heating and cooling provides a strong signal and results in smaller errors. The response cannot be described by downward mixing alone.

For periods between 16 and 2 h in LOTUS, the response turns anticlockwise with depth and exhibits strong surface intensification. A striking feature is the anomalously large response at 25 and 35 m in the LOTUS semidiurnal band. These depths correspond to the buoyancy frequency maximum for the average LOTUS profile, where WKB theory suggests that the response should be amplified. However, such an amplification does not exist at the same depths in other bands. In FASINEX, anticlockwise turning is limited to depths below 20 m. Integrated heating leads surface forcing by a statistically significant margin in both experiments. Failure of the vertically integrated heat balance and upward phase propagation in the response suggest that one-dimensional dynamics are insufficient to describe the response in this band.

At low frequencies, a one-dimensional balance between rate of change of heat and mixing successfully describes the observed response, while the observations are inconsistent with such a model in the two highest frequency bands. In all the high-frequency bands except 16–32 h in LOTUS, the observations fail to satisfy the vertically integrated heat balance (3.3), and the integrated heating consistently leads the surface heat flux. If the dynamics were truly one-dimensional, this balance would be satisfied independent of the details of mixing and stratification. We also expect downward phase propagation if only mixing acts, while in all the highest frequency bands except 32–16 h in FASINEX, the observed sense of propagation is either upward or unclear.

4. Theory

As one-dimensional models cannot explain the high-frequency response, we must consider additional dynamics to understand the observations. Upward phase propagation is consistent with the presence of surface-forced, downward propagating internal gravity waves. We describe buoyancy-forced internal waves using linearized, Boussinesq equations of motion, further simplified by neglecting horizontal mixing and assuming the hydrostatic limit of $\omega \ll N$. This covers the range of our observations, where sampling considerations prevent investigation of the response near the buoyancy frequency. Parameterizing the vertical turbulent fluxes with eddy viscosities and diffusivities, the resulting equations are

$$\rho_0\left(\frac{\partial u}{\partial t} - fv\right) = -\frac{\partial p}{\partial x} + \frac{\partial}{\partial z}\left(A\frac{\partial u}{\partial z}\right) \tag{4.1}$$

$$\rho_0\left(\frac{\partial v}{\partial t} + fu\right) = -\frac{\partial p}{\partial y} + \frac{\partial}{\partial z}\left(A\frac{\partial v}{\partial z}\right) \tag{4.2}$$

$$0 = -\frac{\partial p}{\partial z} - g\rho' \tag{4.3}$$

$$\frac{\partial \rho'}{\partial t} + w\frac{\partial \overline{\rho}}{\partial z} = \frac{\partial}{\partial z}\left(K\frac{\partial \rho'}{\partial z}\right) \tag{4.4}$$

$$\frac{\partial u}{\partial x} + \frac{\partial v}{\partial y} + \frac{\partial w}{\partial z} = 0. \tag{4.5}$$

Here (u, v, w) are eastward, northward, and vertical velocities; A is eddy viscosity; K is eddy diffusivity; p is perturbation pressure; and $\rho(\mathbf{x}, t) = \rho_0 + \overline{\rho}(z) + \rho'(\mathbf{x}, t)$.

A simple analytical model for the upper-ocean response to an oscillatory surface heat flux illustrates how vertical advection in (4.4) alters the response from that predicted by one-dimensional dynamics. Assuming constant eddy diffusivities, constant buoyancy frequency, $N^2 = -(g/\rho_0)\partial\overline{\rho}/\partial z$ and plane wave solutions $\rho' \propto \exp[i(\omega t - kx - ly)]$, (4.1–4.5) yield an equation for the vertical structure of density:

$$\frac{d^8\rho'}{dz'^8} - i2(1 + 2\,\mathrm{Pr}^{-1})\frac{d^6\rho'}{dz'^6} - 4\left(2\,\mathrm{Pr}^{-1} + \frac{\omega^2 - f^2}{\omega^2}\mathrm{Pr}^{-2}\right)\frac{d^4\rho'}{dz'^4} + 4\frac{\omega^2 - f^2}{\omega^2}\mathrm{Pr}^{-2}(i2 - \mathrm{Pr}D^2m^2)\frac{d^2\rho'}{dz'^2} + i8\frac{\omega^2 - f^2}{\omega^2}\mathrm{Pr}^{-2}D^2m^2\rho' = 0. \tag{4.6}$$

Here $\mathrm{Pr} = A/K$ is the Prandtl number, $D = (2K/\omega)^{1/2}$ is the penetration depth, $m = [\kappa_h^2 N^2/(\omega^2 - f^2)]^{1/2}$ is the free internal wave vertical wavenumber, $\kappa_h = \sqrt{k^2 + l^2}$ is the horizontal wavenumber, and $z' = z/D$. We explore solutions for $\mathrm{Pr} \to \infty$, $\mathrm{Pr} \to 0$, and finite Pr.

a. $\mathrm{Pr} \to \infty$, the one-dimensional balance

When eddy diffusivity is much smaller than eddy viscosity, the dynamics are one-dimensional and (4.6) becomes identical in form to (1.1), with solutions described

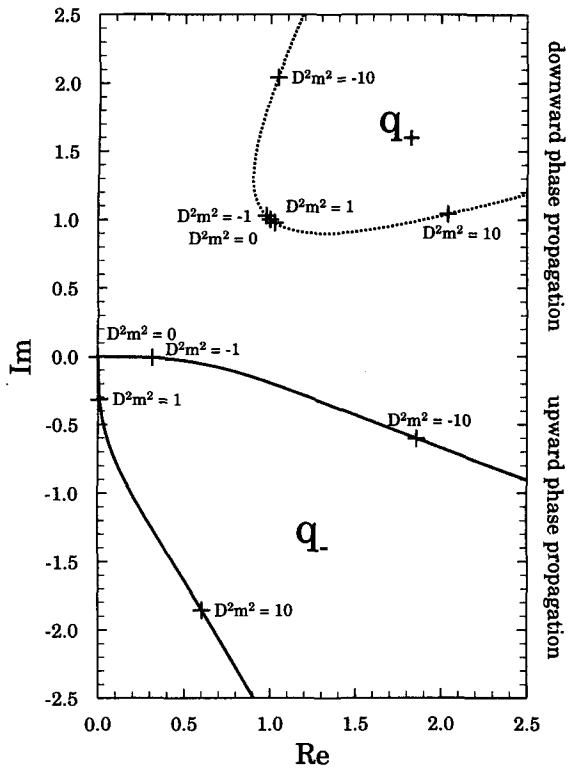

FIG. 7. Plot of q_- and q_+ for $-10 < D^2m^2 < 10$. Solid (q_-) and dashed (q_+) lines trace the complex coefficients as a function of D^2m^2, with selected values marked by crosses.

by (1.2)–(1.3) (Fig. 1). One-dimensional dynamics successfully explain the observations at long timescales but cannot account for the vertically integrated heating and phase propagation of the high-frequency response.

b. $Pr \to 0$, internal wave generation without momentum mixing

Neglecting momentum mixing ($A \to 0$) in (4.1) and (4.2), we derive the simplest model that allows the vertically integrated heating to differ from that predicted using one-dimensional dynamics (1.4). Here vertical advection in (4.4) can generate upward phase propagation and alter the vertically integrated response. The density equation (4.6) becomes

$$\frac{d^4\rho'}{dz'^4} - i2\frac{d^2\rho'}{dz'^2} - i2D^2m^2\rho' = 0. \qquad (4.7)$$

At the surface, we employ the flux boundary condition $(K/D)d\rho'/dz' = Q_0$, where Q_0 is the surface buoyancy flux. For $\omega \ll N$ the free-surface boundary condition reduces to the rigid-lid approximation, $w = 0$, implying $\rho' = -(i/2)d^2\rho'/dz'^2$ at $z' = 0$. The remaining two boundary conditions require that $\rho'(z') \to 0$ and $d\rho'/dz' \to 0$ as $z' \to -\infty$. The solution of (4.7) is

$$\rho'(z') = C_-e^{q_-z'} + C_+e^{q_+z'}, \qquad (4.8)$$

with complex wavenumbers $q_\pm$

$$q_- = \{i[1 - (1 - i2D^2m^2)^{1/2}]\}^{1/2},$$
$$q_+ = \{i[1 + (1 - i2D^2m^2)^{1/2}]\}^{1/2} \qquad (4.9)$$

and complex amplitudes $C_\pm$

$$C_- = \frac{D}{K}\frac{i2 - q_+^2}{i2(q_- - q_+) - q_-q_+^2 + q_+q_-^2}Q_0,$$
$$C_+ = \frac{D}{K}\frac{q_-^2 - i2}{i2(q_- - q_+) - q_-q_+^2 + q_+q_-^2}Q_0. \qquad (4.10)$$

Competition between components with opposing senses of phase propagation determines the relative contributions of mixing and advection in (4.8). Consider the complex coefficients q_- and q_+ as functions of D^2m^2 (Fig. 7). Clockwise (anticlockwise) turning with depth is associated with positive (negative) imaginary parts of q_- and q_+. The magnitude of the imaginary parts governs the rate of turning, while the real parts set the decay scales. When $D^2m^2 = 0$, no waves are generated and only mixing acts, the q_+ solution is identical to (1.2)–(1.3), and the q_- term vanishes. In the internal wave band, $D^2m^2 > 0$ and the q_+ (q_-) solution represents mixing (downward propagating internal waves) with downward (upward) phase propagation and rapid (gradual) decay with depth. The internal wave component dominates with increasing

TABLE 1. Values of D^2m^2 for the frequency bands of the observations in Figs. 5 and 6. Note that D^2m^2 scales directly with eddy diffusivity K, with $K = 1$ m^2 s^{-1} assumed here. Values of D^2m^2 are tabulated for horizontal scales of the atmospheric forcing λ_h ranging from 1000 to 100 km. The FASINEX inertial frequency is $f = 6.62 \times 10^{-5}$ s^{-1} with an average buoyancy frequency of $N = 5.54 \times 10^{-3}$ s^{-1}. LOTUS inertial and average buoyancy frequencies are 8.16×10^{-5} s^{-1} and 1.14×10^{-2} s^{-1} respectively. D^2m^2 is large for forcing at small horizontal scales and changes sign across the inertial frequency.

T (h)	λ_h (km)	D^2m^2 (unitless) FASINEX	LOTUS
2448/3840–360	1000	−0.42	−1.8
360–32	1000	−0.063	−0.18
32–16	1000	0.037	−0.10
16–2	1000	4.0×10^{-4}	1.7×10^{-3}
2448/3840–360	500	−1.7	−7.2
360–32	500	−0.25	−0.71
32–16	500	0.15	−0.41
16–2	500	1.5×10^{-3}	6.9×10^{-3}
2448/3840–360	100	−42	−180
360–32	100	−6.3	−18
32–16	100	3.7	−10
16–2	100	0.038	0.17

D^2m^2. Large values of D^2m^2 result from forcing near the inertial frequency, large diffusivities, such as those expected in mixed layers, and/or forcing at short [O(100 km)] horizontal scales (Table 1). At subinertial frequencies where $D^2m^2 < 0$, the q_- component shows weak phase propagation even for large D^2m^2, and both components decay rapidly with depth.

Compare phase propagation in the observed response to surface heating (Figs. 5 and 6) with hodographs of the rate of change of density predicted by (4.8)–(4.10) (Fig. 8). We consider solutions for $-1 < D^2m^2 < +1$, where $\partial\rho/\partial t$ is analogous to the rate of change of heat coherent with the surface heat flux in (3.1). For $D^2m^2 = 0$, only mixing acts, and we return the solution of (1.1) for density rather than heat (Fig. 1). In the internal wave band (Figs. 8a,b), downward phase propagation near the surface indicates a density balance dominated by mixing, while beneath this phase propagates upward and vertical advection dominates (Fig. 9). Vertical advection increases in importance with increasing D^2m^2. At subinertial frequencies (Figs. 8c,d) solutions to (4.7) are evanescent, no wave generation occurs, and mixing balances the rate of change of density.

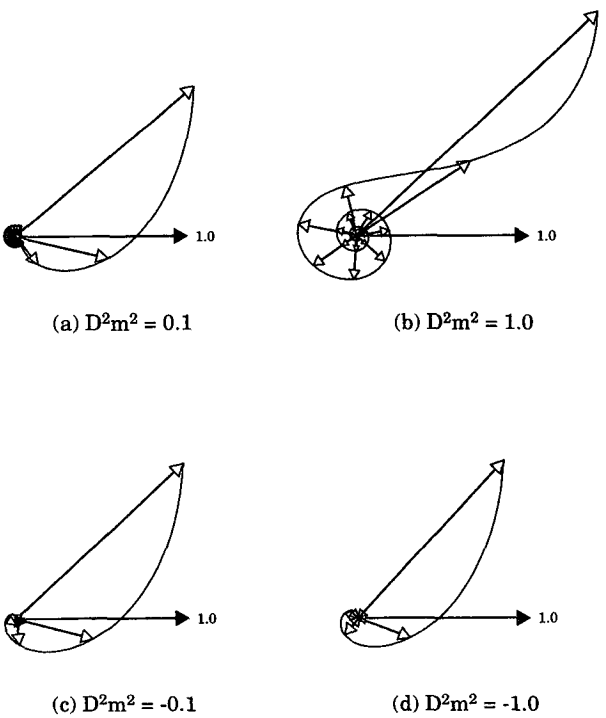

FIG. 8. Hodographs of $\partial\rho'/\partial t$ scaled by $D/Q_0 = (2K/\omega)^{1/2}/Q_0$ from the analytical model forced by surface buoyancy flux. The horizontal arrow with the solid tip is a unit vector in the direction of the real axis. Hollow-tipped vectors mark the solution at integral nondimensional depths between 0 and 10 and the curve connecting the tips traces $\partial\rho'/\partial t$ as a function of depth. The size of the arrowheads decreases with depth. Upward phase propagation is indicated by anticlockwise turning of the response with depth, while for downward phase propagation the sense of turning is reversed. Each hodograph is for a different value of D^2m^2. (a) and (b) Solutions for $f < \omega < N$ in the internal wave band where $D^2m^2 > 0$. (c), (d) Solutions for $f > \omega$, outside the internal wave band where $D^2m^2 < 0$.

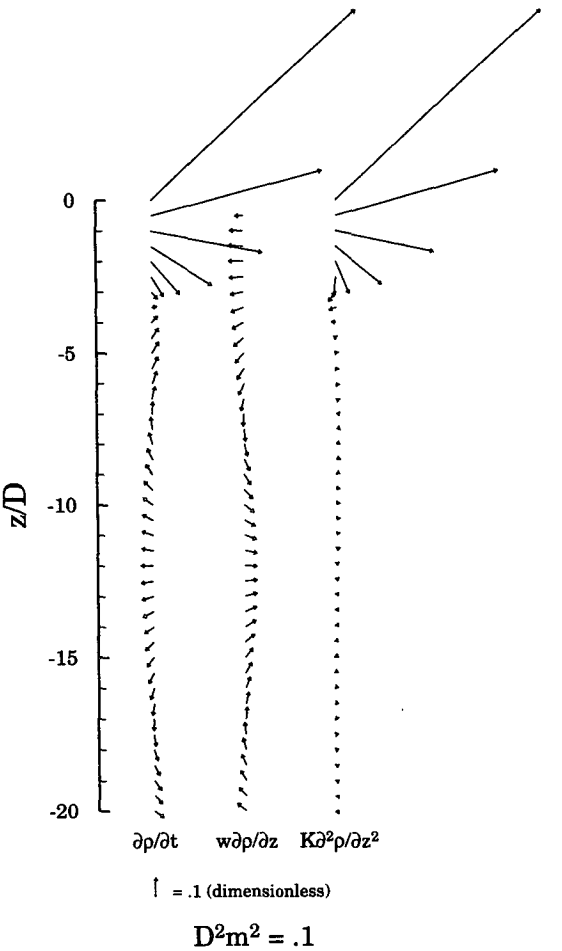

FIG. 9. Vertical profiles of $\partial\rho'/\partial t$, $w\partial\bar{\rho}/\partial z'$, and $K\partial^2\rho'/\partial z'^2$ scaled by $D = (2K/\omega)^{1/2}$ from the analytical model with $D^2m^2 = 0.1$. The three terms are plotted for nondimensional depths $z' = z(\omega/2K)^{1/2}$ between 0 and 20 as vectors in the complex plane. A scale arrow at the bottom of the frame indicates a value of 0.1 in the direction of the imaginary axis. Upward phase propagation is displayed by $w\partial\bar{\rho}/\partial z'$ and downward phase propagation by $K\partial^2\rho'/\partial z'^2$. Mixing dominates the balance over the upper three penetration depths, below which vertical advection becomes important and the sense of phase propagation reverses.

Vertical advection consistently results in an anticlockwise phase shift from the vertically integrated rate of change of density expected if only mixing were acting. Vertically integrating (4.4) and applying the surface flux condition yields

$$\frac{1}{Q_0}\int_{-\infty}^{0}\frac{\partial\rho'}{\partial t}\,\partial z = 1 - \frac{1}{Q_0}\int_{-\infty}^{0} w\frac{\partial\bar{\rho}}{\partial z}\,\partial z. \quad (4.11)$$

The degree to which the integrated balance is modified

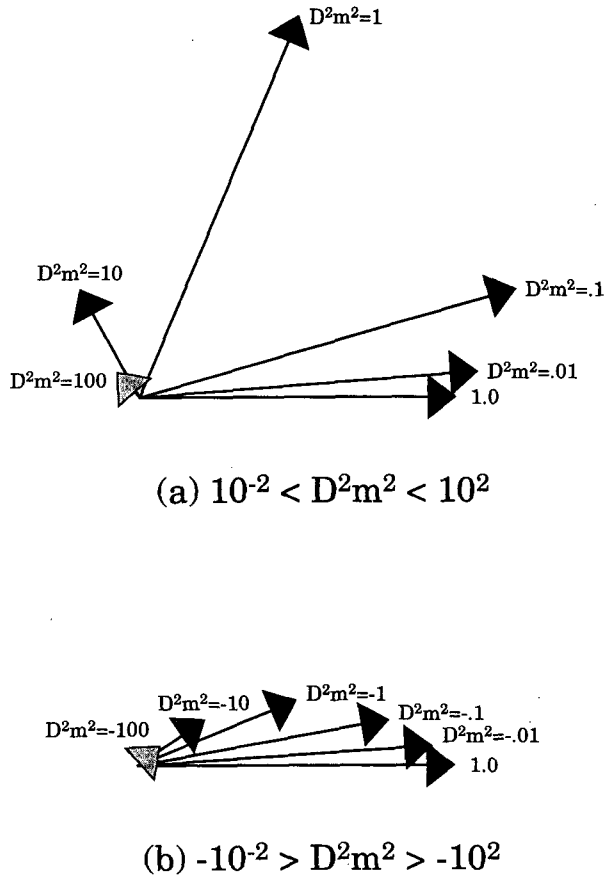

FIG. 10. Vertically integrated $(1/Q_0)\partial\rho'/\partial t$ for the analytical model plotted as a function of D^2m^2. The horizontal arrow with the solid tip is a unit vector in the direction of the real axis. Vertically integrated rate of change of density for different values of D^2m^2 are plotted as vectors with shaded tips, where the darkest corresponds to the smallest value of D^2m^2 in the group and the lightest to the largest. At $D^2m^2 = 0$, only mixing acts and the integrated rate of change of density equals the scale arrow. (a) Integrated rate of change of density for $10^{-2} < D^2m^2 < 10^2$ with vectors plotted for each power of 10. (b) Integrated rate of change of density for $-10^{-2} > D^2m^2 > -10^2$ with vectors plotted for each power of 10.

is a function of D^2m^2 (Fig. 10). At $D^2m^2 = 0$, the second term on the right-hand side of (4.11) vanishes, and this becomes an analog of (1.4) for the one-dimensional density balance. Vertical advection causes an anticlockwise phase shift and a slight overresponse with increasing D^2m^2 in the internal wave band. At large D^2m^2 the integrated rate of change of density is smaller than is expected from mixing alone, and as $D^2m^2 \to \infty$, phase approaches $3\pi/4$ and magnitude approaches zero. Outside the internal wave band, phase shifts are anticlockwise, with magnitude vanishing and phase approaching $\pi/4$ as $D^2m^2 \to -\infty$. All nonzero values of D^2m^2 produce anticlockwise phase shifts similar to those present in the observed vertically integrated heating (Figs. 5 and 6, bottom row).

c. *Finite Pr, internal wave generation with momentum mixing*

In the more realistic case where buoyancy and momentum mix in a similar manner, momentum mixing dissipates buoyancy-forced internal waves near the surface. As the Prandtl number increases, wave generation is damped, and the response shifts from a partition between vertical advection and mixing ($\mathrm{Pr} \to 0$, section 3b) to mixing alone ($\mathrm{Pr} \to \infty$, section 3a). Surface and bottom flux conditions on the horizontal momentum equations provide the additional boundary conditions required to solve (4.6). The solution is

$$\rho'(z') = C_- e^{q_- z'} + C_{1+} e^{q_{1+} z'} + C_{2+} e^{q_{2+} z'} + C_{3+} e^{q_{3+} z'}, \quad (4.12)$$

where complex wavenumbers q_-, q_{1+}, q_{2+}, and q_{3+} are those roots of the characteristic equation having positive real parts and the amplitudes C_-, C_{1+}, C_{2+}, and C_{3+} are determined using the four surface boundary conditions. For $D^2m^2 = 0.1$ and $\mathrm{Pr} = .01$, both mixing and vertical advection balance the rate of change of density (Fig. 11a), and the solution is indistinguishable from that for $\mathrm{Pr} = 0$ (Fig. 8a). For $\mathrm{Pr} = 1$ (Fig. 11b), vertical advection weakens and the mixing term grows in importance, though upward phase propagation is still apparent. The reversal in the sense of phase propagation occurs deeper for larger Prandtl number. By $\mathrm{Pr} = 100$ (Fig. 11c), mixing dominates the response to surface heating, and essentially no wave generation occurs.

d. *Summary*

Vertical advection explains two features of the observations for which one-dimensional models cannot account: anticlockwise displacement of the vertically integrated heating and upward phase propagation in the response. Near the surface, mixing balances the rate of change of density, and the response takes the form of a heating spiral with downward phase propagation. The presence of upward phase propagation indicates a balance primarily between the rate of change and vertical advection and represents internal waves forced by surface heat flux propagating away from the region of generation. A distinct reversal of the phase spiral marks this shift in the density balance. In cases where vertical advection is an important component of the density balance, the depth-integrated response shows a consistent anticlockwise phase shift relative to that expected when mixing alone acts. Momentum mixing inhibits internal wave generation, and at large Prandtl number internal waves generated by surface buoyancy forcing quickly dissipate. More complex models employing depth-dependent diffusivities produce similar results.

5. Diffusivities and length scales

Although the models presented in section 4 predict the correct sense of phase propagation, we fit them to

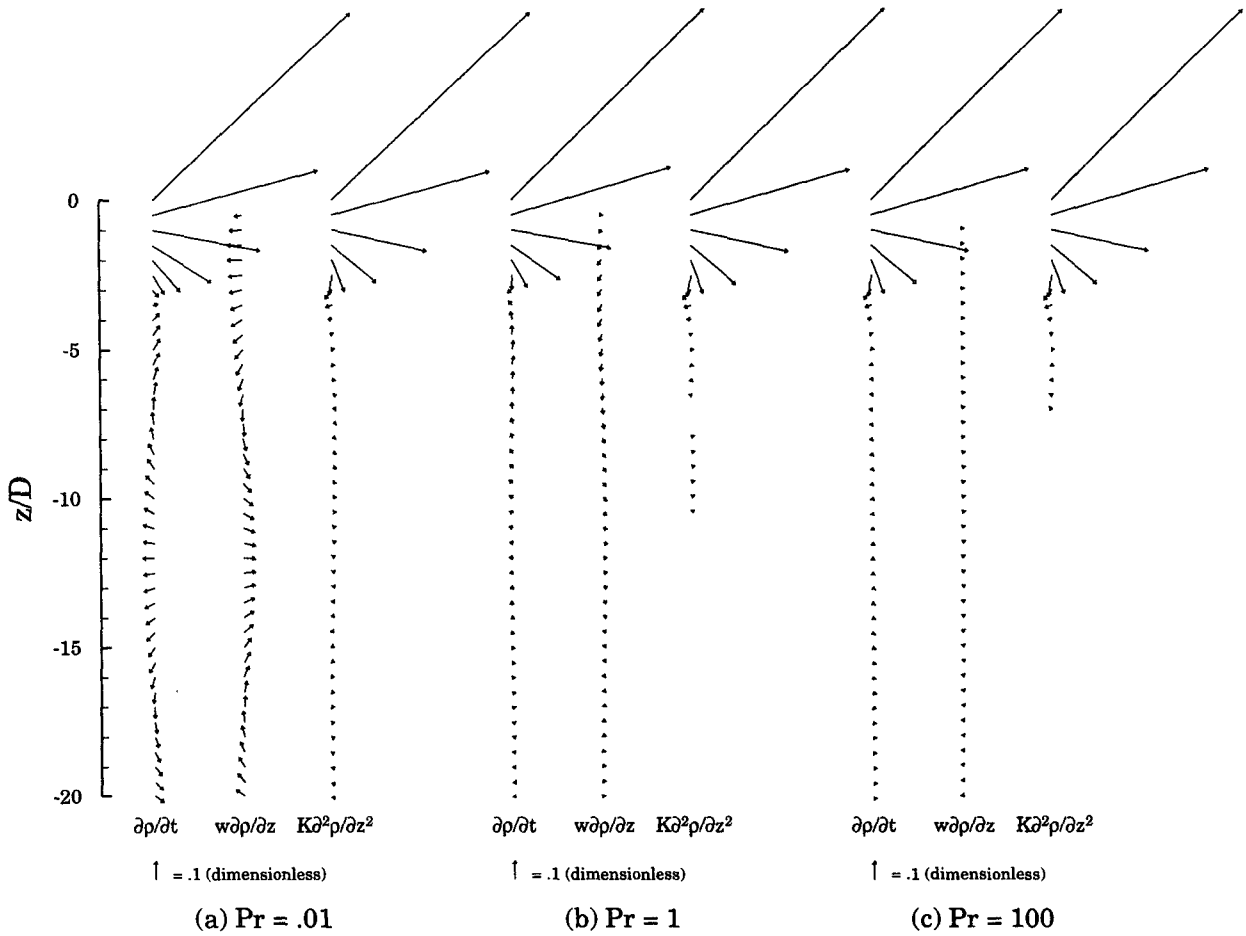

FIG. 11. Vertical profiles of $\partial\rho'/\partial t$, $w\partial\bar{\rho}/\partial z'$, and $K\partial^2\rho'/\partial z'^2$ scaled by $D = (2K/\omega)^{1/2}$ from the finite Prandtl number model (4.7) with $D^2m^2 = 0.1$ displayed in the same manner as Fig. 9. (a) Pr = .01 and the response is indistinguishable from that when Pr = 0 and the mixing of momentum is neglected. As Prandtl number increases, wave generation is damped and at Pr = 1 (b) the amplitude of $w\partial\bar{\rho}/\partial z'$ is significantly reduced and the waves dissipate quickly with depth. By Pr = 100 (c) the upper-ocean density balance is primarily between rate of change and mixing.

the observed response to determine whether they imply plausible diffusivities and length scales. We estimate diffusivities K and horizontal forcing scales L for individual frequency bands by minimizing the square misfit between the observed transfer functions (Figs. 5 and 6) and a modeled response. The misfit error is

$$E(\omega, K) = \sum_{i=1}^{N} \left\| H_Q(z_i, \omega) - \frac{i\omega\rho_0 c_p}{\tilde{Q}_0(\omega)} \tilde{T}(z_i, \omega) \right\|^2, \quad (5.1)$$

where N is the number of transfer function estimates $H_Q(z_i, \omega)$ (3.2) and z_i are the depths of the estimates; $\tilde{T}(z_i, \omega)$ is the theoretical response to oscillatory surface heat flux $\tilde{Q}_0(\omega)$, calculated using the models described above. The downhill simplex method (Press et al. 1993) minimizes misfit (5.1) with parameter errors estimated as detailed in the appendix.

We first estimate the diffusivity implied by the heat diffusion equation (1.1). Diffusivities range from 54 $cm^2\ s^{-1}$ in the highest to 3 $cm^2\ s^{-1}$ in the lowest frequency band of LOTUS and from 230 $cm^2\ s^{-1}$ in the semidiurnal band to 31 $cm^2\ s^{-1}$ in the next-to-lowest band in FASINEX (Table 2a). Diffusivity must vary with frequency, as frequency-independent diffusivity implies infinite penetration depth as $\omega \to 0$ and cannot explain the surface trapping observed across all timescales (Figs. 5 and 6). Advection contaminates the FASINEX response at the longest timescales, and we obtain an anomalously high diffusivity with large error. LOTUS diffusivities are less than half the size of their FASINEX counterparts, reflecting stronger surface trapping of the response. Upward phase propagation, a promi-

TABLE 2. Estimates of eddy diffusivities and length scales based on the observations of section 3 and models of section 4. One standard deviation errors ϵ_K and ϵ_L are calculated as described in the appendix, and the misfit E between the observed and modeled response is listed for each estimate. (a) Eddy diffusivity K ($m^2\ s^{-1}$) based on the one-dimensional heat diffusion equation (1.1) with depth-independent diffusivity. (b) Eddy diffusivity K ($m^2\ s^{-1}$) and horizontal forcing scale L (km) from a dimensional version of (4.7) assuming Pr = 1.

(a) Pr = ∞, the one-dimensional balance

Period (h)	K	ϵ_K	E
	LOTUS		
3828–360	2.6×10^{-4}	1.4×10^{-4}	3.9×10^{-3}
360–32	9.2×10^{-4}	4.4×10^{-4}	4.7×10^{-3}
32–16	3.6×10^{-3}	7.5×10^{-4}	7.6×10^{-3}
16–2	5.4×10^{-3}	6.6×10^{-4}	5.0×10^{-2}
	FASINEX		
2448–360	8.6×10^{-1}	6.0×10^{0}	4.0×10^{-3}
360–32	3.1×10^{-3}	1.0×10^{-3}	3.1×10^{-4}
32–16	1.1×10^{-2}	1.5×10^{-3}	1.3×10^{-3}
16–2	2.3×10^{-2}	1.9×10^{-3}	5.3×10^{-3}

(b) Pr = 1, internal wave generation with momentum mixing

	K	ϵ_K	L	ϵ_L	E
	LOTUS				
3828–360	2.7×10^{-4}	1.3×10^{-4}	∞	—	3.9×10^{-3}
360–32	9.2×10^{-4}	4.2×10^{-4}	∞	—	4.7×10^{-3}
32–16	3.9×10^{-3}	6.9×10^{-4}	16	6.6	6.7×10^{-3}
16–2	6.7×10^{-3}	1.5×10^{-3}	4.6	1.8	4.2×10^{-2}
	FASINEX				
2448–360	8.6×10^{-1}	6.6×10^{1}	∞	—	4.0×10^{-3}
360–32	3.1×10^{-3}	9.5×10^{-4}	∞	—	3.1×10^{-4}
32–16	1.1×10^{-2}	1.6×10^{-3}	29	11	1.2×10^{-3}
16–2	2.4×10^{-2}	1.7×10^{-3}	6.4	1.4	4.6×10^{-3}

nent feature of the high-frequency observations, cannot be reproduced by this model.

Fitting the internal wave model (4.6) produces short horizontal forcing scales with diffusivities similar to those indicated by one-dimensional dynamics. The values obtained with Pr = 0 and Pr = 1 are indistinguishable from each other, and we tabulate only the results for Pr = 1 (Table 2b). In the two lowest frequency bands, wave generation plays no role in the response, and we find essentially infinite horizontal forcing scales with diffusivities and misfits identical to those obtained from the heat diffusion equation. In the highest two frequency bands, the observations indicate extremely short horizontal forcing scales of $O(10$ km), implying $D^2m^2 > 0.1$ with modest improvements in the misfit. Our model correctly captures the sense of phase propagation in the diurnal and semidiurnal bands (Figs. 5 and 6). However, the observed phase changes occur very rapidly with depth, and the model cannot reproduce these short vertical wavelengths given plausible forcing parameters. A possible explanation is that we have oversimplified the dynamics by considering only the linearized vertical advection, while in the fully nonlinear case density fluctuations with short vertical scales should add short-scale variability to the response.

Eddy diffusivity may be described as a linear function of frequency where the scaling constant reflects the mixed layer depth. Diffusivities vary by an order of magnitude across the frequencies considered, with the largest values associated with high frequencies. Neglecting the lowest frequency band in FASINEX due to contamination, plotting K against ω (Fig. 12) yields points falling on essentially straight lines. Expressing eddy diffusivity as $K = (D^2/2)\omega$, least squares estimates of the slopes yield e-folding depths D and one standard deviation error of 7.2 − 8.1 m (±4 m) and 14.6 − 15.0 m (±5 m) for LOTUS and FASINEX respectively. Diffusive e-folding scales are approximately one-third the time-averaged mixed layer depth in each experiment, emphasizing the role of stratification in limiting the penetration depth of turbulent mixing. The vertical scale of the observed response is model independent, and an alternative parameterization of the turbulent flux should rely on similar scaling.

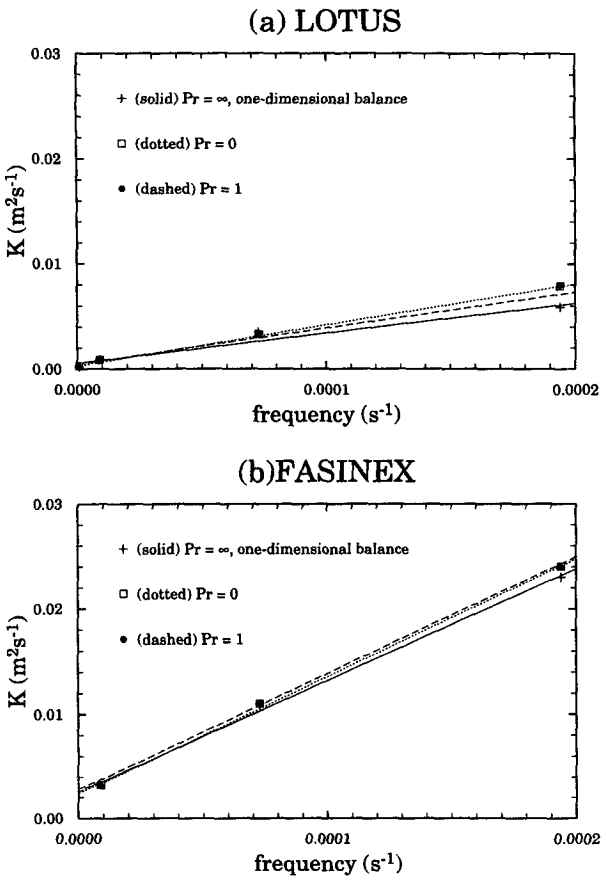

FIG. 12. Estimates of eddy diffusivity plotted against frequency for (a) LOTUS and (b) FASINEX. Lines represent linear fits of diffusivity as a function of frequency. Crosses and solid lines mark the heat diffusion model, squares and dotted lines the Pr = 0 model, and dots and dashed lines the Pr = 1 case. We calculate e-folding depths and one standard deviation errors from the line slopes m_{slope} as $D = (2m_{slope})^{1/2}$. LOTUS e-folding depths are 7.2 ± 2.7 m, 8.2 ± 4 m, and 8.1 ± 4 m and FASINEX depths are 15 ± 4.9 m, 15 ± 6.4 m, and 15 ± 4.7 m for the three models.

6. Discussion and conclusions

One-dimensional dynamics accurately model the upper-ocean response to surface heating at low frequencies but fail to account for key features of the internal wave band observations. At long timescales, the observed response (Figs. 5 and 6, two leftmost columns) satisfies the vertically integrated heat balance (3.3), exhibits downward phase propagation, and decays with depth. The exception is the FASINEX low-frequency response, where we believe strong horizontal advection contaminates our analysis. Satisfaction of the vertically integrated heat equation indicates that mixing balances the rate of change of heat (1.1), and the response predicted by a simple diffusive model (Fig. 1) compares favorably with the observed heating spirals. At shorter timescales (Figs. 5 and 6, two rightmost columns), the observed vertically integrated heating shows a distinct, anticlockwise phase shift, which cannot be explained using one-dimensional dynamics. The high-frequency response also exhibits upward phase propagation, where one-dimensional models predict only downward phase propagation. Errors in the observed response and its integral are small enough that phase differences are significant and may not be dismissed as noise.

Vertical advection can explain upward phase propagation and anticlockwise phase shifts in the integrated response. As one-dimensional dynamics exclude advection, we illustrate this using a more complete linear model (4.6), where the upper ocean responds to buoyancy forcing through mixing and internal wave generation. Model results in the internal wave band (Figs. 8a,b and 10a) and the observed high-frequency response (Figs. 5 and 6, two rightmost columns) show similar phase structures and vertical integrals. Near the surface, mixing dominates the response and phase propagates downward, similar to the heating spiral of the one-dimensional model. Deeper, vertical advection dominates and the sense of phase propagation reverses. This is the signature of downward propagating, buoyancy-forced internal waves. Vertical advection modifies the integrated heating (4.11) and results in an anticlockwise phase shift from that predicted by one-dimensional models (1.4), consistent with the observations reported above.

Although our model predicts the correct sense of phase propagation, achieving the right magnitude is problematic. The observed rate of phase change implies unrealistically short horizontal forcing scales. This problem may arise from the linearization of vertical advection, which neglects diurnal cycling and other sources of temporal variability in stratification. In a model employing the true vertical advection, variability in both the forcing and the stratification sets the vertical scale of the response.

Eddy diffusivity is a linear function of frequency $K = (D^2/2)\omega$, where the e-folding depth D scales with the mixed layer depth (Fig. 12). The observed response yields e-folding scales of 8 and 15 m, roughly one-third the average mixed layer depth for LOTUS and FASINEX respectively. This implies that stratification sets an underlying length scale for the vertical mixing of heat. Estimates of vertical profiles of diffusivity provided no additional insight.

One-dimensional mixed layer models incorporating the diurnal cycle of stratification can explain many features of the upper ocean (Davis et al. 1981b; Price et al. 1986; Schudlich and Price 1995). In these models, coherence between mixed layer depth and surface forcing produces vertical decay and phase structure in the mean, but cannot alter the vertically integrated heating from that specified by (1.4). However, given more complete dynamics, the diurnal cycle may play an important role in setting the true vertical advection, thus altering the vertically integrated heat balance. We have not considered this effect,

and the need for a more accurate representation of vertical advection should guide further developments.

In a simplified framework, we explain the upper-ocean response to surface heating as a balance between the rate of change of heat, mixing, and vertical advection (4.4). Magaard (1973) briefly examines internal wave generation by an oscillatory surface buoyancy flux. Although he finds that wind forcing drives a larger internal wave response, he notes that buoyancy forcing remains significant in light to moderate winds. The response predicted by a model that includes internal wave generation compares favorably with our observations. Vertical advection of the background stratification produces upward phase propagation and modifies the vertically integrated heating. Altering the mixing parameterization should not significantly change these results, but incorporating the effects of time-varying stratification on vertical advection would greatly improve the model.

Acknowledgments. We thank Robert Weller for generously providing the observations used in this study. Charles Eriksen, Eric Kunze, LuAnne Thompson, Emmanuel Boss, Dan Codiga, and Joanna Muench, and an anonymous reviewer made helpful comments on the manuscript. We gratefully acknowledge the support of the Office of Naval Research through Contracts N00014-89-J-1621 (CML) and N00014-90-J-1496 (DLR).

APPENDIX

Error Estimates for a Nonlinear Optimization

We derive an expression for the one standard deviation errors of the diffusivity estimates by taking a Taylor expansion of the nonlinear inverse about the solution. Consider the general nonlinear inverse $g(\mathbf{m}) = \mathbf{d}$, where some function g of parameter vector $\mathbf{m}$ models data vector $\mathbf{d}$. Define $\mathbf{m}_0$ as the optimal estimate of the parameter vector, $\Delta\mathbf{m}$ as the parameter error variance, and $\Delta\mathbf{d}$ as the data error variance, where $g(\mathbf{m} + \Delta\mathbf{m}) = \mathbf{d} + \Delta\mathbf{d}$. Expanding $g(\mathbf{m} + \Delta\mathbf{m})$ about $\mathbf{m}_0$ and retaining the zeroth- and first-order terms, the linearized parameter error variance may be expressed as

$$\langle \Delta\mathbf{m}\Delta\mathbf{m}^t \rangle = (J(g, \mathbf{m})^t J(g, \mathbf{m}))^{-1} J(g, \mathbf{m})^t \langle \Delta\mathbf{d}\Delta\mathbf{d}^t \rangle \times J(g, \mathbf{m})(J(g, \mathbf{m})^t J(g, \mathbf{m}))^{-1t}, \quad \text{(A.1)}$$

where angle brackets indicates averaging and $J(g, \mathbf{m})$ is a Jacobian. We assume that errors in the transfer functions are uncorrelated with each other and $\langle \Delta\mathbf{d}\Delta\mathbf{d}^t \rangle$ is thus a diagonal matrix composed of the squares of the transfer function standard errors. We take the diagonal of $\langle \Delta\mathbf{m}\Delta\mathbf{m}^t \rangle$ as an estimate of the parameter error variance.

REFERENCES

Bendat, J. S., and A. G. Piersol, 1986: *Random Data: Analysis and Measurement Procedures.* 2d ed. John Wiley and Sons, 566 pp.

Bowden, K. F., M. R. Howe, and R. I. Tait, 1970: A study of the heat budget over a seven-day period at an ocean station. *Deep-Sea Res.,* **17,** 401–411.

Briscoe, M. G., and R. A. Weller, 1984: Preliminary results from the Long-Term Upper-Ocean Study (LOTUS). *Dyn. Atmos. Oceans,* **8,** 243–265.

Chereskin, T. K., and D. Roemmich, 1991: A comparison of measured and wind-driven Ekman transport at 11°N in the Atlantic Ocean. *J. Phys. Oceanogr.,* **21,** 869–878.

Davis, R. E., R. DeSzoeke, D. Halpern, and P. Niiler, 1981a: Variability in the upper ocean during MILE. Part I: The heat and momentum balances. *Deep-Sea Res.,* **28A,** 1427–1451.

——, ——, and P. Niiler, 1981b: Variability in the upper ocean during MILE. Part II: Modeling the mixed layer response. *Deep-Sea Res.,* **28A,** 1453–1475.

Deser, C., R. A. Weller, and M. G. Briscoe, 1983: Long Term Upper Ocean Study (LOTUS) at 34°N, 70°W: Meteorological sensors, data, and heat fluxes for May–October 1982 (LOTUS-3 and LOTUS-4). Woods Hole Oceanographic Institution Tech. Rep. WHOI 83-32, Woods Hole Oceanographic Institute, 68 pp.

Faller, A. J., and R. Kaylor, 1969: Oscillatory and transitory Ekman boundary layers. *Deep-Sea Res.,* **16,** 45–58.

Halpern, D., and R. K. Reed, 1976: Heat budget of the upper ocean under light winds. *J. Phys. Oceanogr.,* **6,** 972–975.

Isemer, H.-J., and L. Hasse, 1985: *The Bunker Climate Atlas of the North Atlantic Ocean.* Vol. 1. 1st ed. Springer Verlag, 218 pp.

Magaard, L., 1973: On the generation of internal gravity waves by a fluctuating buoyancy flux at the sea surface. *Geophys. Fluid Dyn.,* **5,** 101–111.

Paulson, C. A., and J. J. Simpson, 1977: Irradiance measurements in the upper ocean. *J. Phys. Oceanogr.,* **7,** 952–956.

Press, W. H., B. P. Flannery, S. A. Teukolsky, and W. T. Vetterling, 1993: *Numerical Recipes in C.* 2d ed. Cambridge University Press, 994 pp.

Price, J. A., R. A. Weller, and R. Pinkel, 1986: Diurnal cycling: Observations and models of the upper-ocean response to diurnal heating, cooling and wind mixing. *J. Geophys. Res.,* **91,** 8411–8427.

——, ——, and R. R. Schudlich, 1987: Wind-driven ocean currents and Ekman transport. *Science,* **238,** 1534–1538.

Rudnick, D. L., and R. A. Weller, 1993a: The heat budget of the North Atlantic Subtropical Frontal Zone. *J. Geophys. Res.,* **98,** 6883–6893.

——, and ——, 1993b: Observations of superinertial and near-inertial wind-driven flow. *J. Phys. Oceanogr.,* **23,** 2351–2359.

Schudlich, R. R., and J. F. Price, 1995: Observations of seasonal variation in the Ekman layer. *J. Phys. Oceanogr.,* submitted.

Shonting, D. H., 1964: Some observations of short-term heat transfer through the surface layers of the ocean. *Limnol. Oceanogr.,* **9,** 576–588.

Sverdrup, H. U., M. W. Johnson, and R. H. Fleming, 1942: *The Oceans.* 1st ed. Prentice-Hall, 1087 pp.

Weller, R. A., D. L. Rudnick, R. E. Payne, J. P. Dean, N. J. Pennington, and R. P. Trask, 1990a: Measuring near-surface meteorology over the ocean from an array of surface moorings in the subtropical convergence zone. *J. Atmos. Oceanic Technol.,* **7,** 85–103.

——, ——, N. J. Pennington, R. P. Trask, and J. R. Valdes, 1990b: Measuring upper ocean variability from an array of surface moorings in the subtropical convergence zone. *J. Atmos. Oceanic Technol.,* **7,** 68–84.

——, ——, C. C. Eriksen, K. L. Polzin, N. S. Oakey, J. W. Toole, R. W. Schmitt, and R. T. Pollard, 1991: Forced ocean response during the frontal air–sea interaction experiment. *J. Geophys. Res.,* **96,** 8611–8638.